15. J. V. Naidich, in *Progress in Surface and Membrane Science*, D. A. Cadenhead, C. F. Danielli, Eds. (Academic Press, New York, 1981), vol. 14, pp. 353–484.
16. I. Egry, G. Lohoefer, G. Jacobs, *Phys. Rev. Lett.* **75**, 4043 (1995).
17. C. Ukiwe, D. Y. Kwok, *Langmuir* **21**, 666 (2005).
18. We are grateful for the experimental contributions by S. Rottmair at the early stages of this work. We acknowledge financial support by the Deutsche Forschungsgemeinschaft within the SFB 513, Project B1 and the Landesstiftung Baden-Württemberg

# The Global Reach of the 26 December 2004 Sumatra Tsunami

Vasily Titov,[1]* Alexander B. Rabinovich,[2,3] Harold O. Mofjeld,[1] Richard E. Thomson,[2] Frank I. González[1]

Numerical model simulations, combined with tide-gauge and satellite altimetry data, reveal that wave amplitudes, directionality, and global propagation patterns of the 26 December 2004 Sumatra tsunami were primarily determined by the orientation and intensity of the offshore seismic line source and subsequently by the trapping effect of mid-ocean ridge topographic waveguides.

At 07:59 local time (00:59 UTC) on 26 December 2004, a moment magnitude ($M_w$) 9.3 megathrust earthquake occurred along 1300 km of the oceanic subduction zone located 100 km west of Sumatra and the Nicobar and Andaman Islands in the eastern Indian Ocean (*1*). Highly destructive waves were generated by up to 10-m vertical displacements associated with massive (more than 20 m horizontally), sudden movements of adjacent plates during this event (*2, 3*). Hundreds of thousands of dead and billions of dollars in damage show the catastrophic regional impact of this tsunami. At the same time, the waves recorded around the world revealed unprecedented, truly global reach of the waves generated on 26 December (Fig. 1). This tsunami is the first for which there are high-quality worldwide tide-gauge measurements and for which there are multiple-satellite altimetry passes of tsunami wave height in the open ocean. In this study, we couple global observations with numerical simulations to determine the principal factors affecting that portion of seismic energy that was transported thousands of kilometers throughout the world ocean in the form of tsunami waves.

We focus on measurements in intermediate and far-field regions (Fig. 2) to characterize the worldwide distribution of magnitudes and general propagation characteristics of the Sumatra tsunami. Although coastal tide-gauge records are available for much of the world ocean, interpretation of this data is compli-

cated because of their varied quality. For example, the sampling rate for Pacific Ocean gauges is generally 15 s to 2 min, but it is only 2 to 30 min for the more sparse observations in the Indian Ocean and 6 to 15 min for the Atlantic Ocean, including the well-instrumented U.S. East Coast.

The first instrumental tsunami measurements were available about 3 hours after the earthquake from the real-time reporting tide gauge at the Cocos Islands (Fig. 1), located approximately 1700 km from the epicenter (*4*). Data from this gauge (Fig. 2A) reveal a 30-cm-high first wave followed by a long train of water-level oscillations with maximum peak-to-trough ranges of 53 cm. Gauge data and run-up measurements from sites in India and Sri Lanka (*5*) at similar distances from the epicenter yielded amplitudes almost 10 times as high as the Cocos Islands values. These substantial wave-height differences are consistent with numerical modeling results that clearly demonstrate the highly directional nature of the Sumatra tsunami (Fig. 1). Data from other tide gauges around the Indian Ocean show amplitudes ranging from about 3 m to less than 0.5 m, with no well-defined attenuation with distance from the source. Similarly, gauge wave heights are not necessarily correlated with the heights of tsunami inland inundation (run-up) in the vicinity of the gauge. The few tide-gauge records available for areas with substantial inundation show recorded water elevations smaller by a factor of 2 to 5 than measured tsunami run-up in the same area. For example, at Chenai, 1.5 m at the gauge translated into a 3- to 4-m run-up, whereas 1.5 m at Phuket gauge was a 3- to 6-m run-up. This well-known discrepancy (*6*) complicates determination of the true tsunami heights from coastal data. Many of the gauges in the Indian Ocean region were either destroyed (e.g., Thailand) or malfunctioned (e.g., Colombo, Sri Lanka), so that the largest amplitudes may not have been recorded.

Data from regions outside the Indian Ocean (Fig. 2) present an even more complex picture of tsunami behavior. The measurements indicate that, contrary to near-field regions, maximum tsunami wave heights were not associated with the leading waves. In the North Atlantic and North Pacific, maximum waves arrived several hours to 1 day after the initial tsunami (*7*). Furthermore, larger tsunami amplitudes were recorded at Callao, Peru, 19,000 km east of the epicenter than at the Cocos Islands 1700 km to the south of the epicenter. Similarly, wave amplitudes at Halifax, Nova Scotia, were also greater than at the Cocos Islands, even though these waves had propagated more than 24,000 km west across the Indian Ocean and then north along the entire length of the South and North Atlantic Ocean.

Satellite altimetry measurements of tsunami amplitude—corrected for quasi-permanent ocean circulation features such as eddies—were obtained from the Jason-1 and Topex/Poseidon satellites as they transited the Indian Ocean ~150 km apart about 2 hours after the quake (*8, 9*). The tracks crossed the spreading front of the tsunami waves in the Bay of Bengal down to about 1200 km southward from Sri Lanka. The measurements revealed amplitudes of about 50 to 70 cm of the leading tsunami wave at this location of the Indian Ocean.

To interpret and study such a complex data set, we have employed the rigorously tested MOST (method of splitting tsunami) model (*10*) to simulate worldwide tsunami propagation. Figure 1 summarizes simulation results for a model tsunami source constrained by the open-ocean satellite measurements and available seismic analysis. The slip distribution between the subfaults of our source provides the best fit with the open-ocean satellite data and qualitatively agrees with the magnitude of the earthquake source data (Fig. 1, inset). The details of the coseismic deformation that generated these powerful waves still have substantial uncertainties. The ambiguities and difficulties of interpreting the distinctive seismic data for this event are reflected in substantially different source models derived from the seismic data (*4, 11*). Geodetic field measurements and Global Positioning System data provide another source interpretation (*3*). The tsunami data provide considerable insight into the large-scale source structure, because they reflect extremely low-frequency source characteristics. Inversion studies of the satellite tsunami data offer yet another version of the source (*12*). For our study, however, the small-scale features of the tsunami source may not be criti-

[1]Pacific Marine Environmental Laboratory, National Oceanic and Atmospheric Administration, Sand Point Way NE, Seattle, Washington 98115, USA. [2]Institute of Ocean Sciences, Department of Fisheries and Oceans Canada, 9860 West Saanich Road, Sidney, British Columbia, Canada V8L 4B2. [3]P. P. Shirshov Institute of Oceanology, Russian Academy of Sciences, 36 Nakhimovsky Prospect, Moscow 117997, Russia.

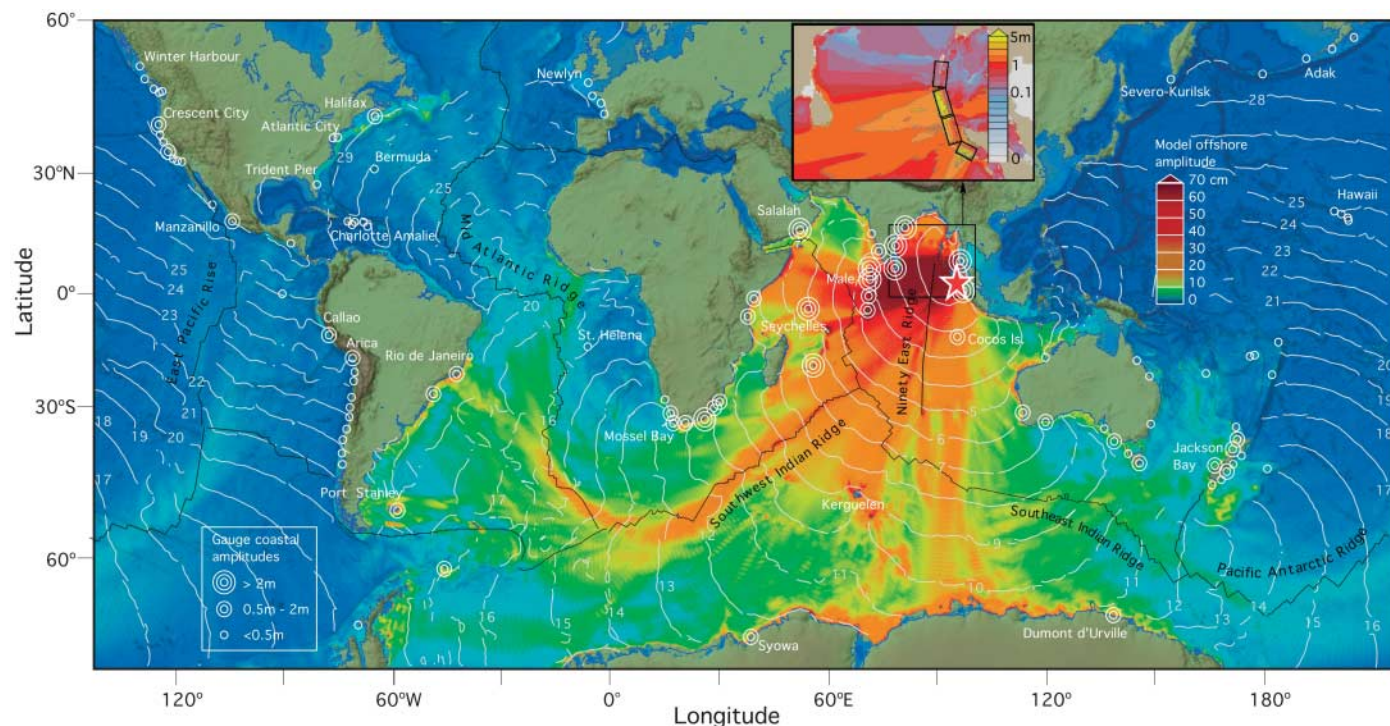*To whom correspondence should be addressed. E-mail: Vasily.Titov@noaa.gov

**Fig. 1.** Global chart showing energy propagation of the 2004 Sumatra tsunami calculated from MOST. Filled colors show maximum computed tsunami heights during 44 hours of wave propagation simulation. Contours show computed arrival time of tsunami waves. Circles denote the locations and amplitudes of tsunami waves in three range categories for selected tide-gauge stations. Inset shows fault geometry of the model source and close-up of the computed wave heights in the Bay of Bengal. Distribution of the slip among four subfaults (from south to north: 21 m, 13 m, 17 m, 2 m) provides best fit for satellite altimetry data and correlates well with seismic and geodetic data inversions.

cal, because tsunami propagation patterns away from the source are not very sensitive to such details. The magnitude of seafloor displacement, aerial extent of displacement, and its location are the most critical source parameters determining characteristics of the far-field tsunami propagation (*13*). Consequently, our model results in Fig. 1 are qualitatively similar to the early MOST model obtained only hours after the earthquake, which used substantially simpler source assumptions not constrained by later data analysis (*14*) (fig. S1 and movie S1). The magnitude ($M_w = 9.2$) and dimensions of our model source are consistent in general with seismic and geodetic inversions, and it fits well the tsunami altimetry measurements, thus providing a robust model for worldwide propagation.

Model simulations of tsunamis provide insight into open-ocean wave propagation that cannot be determined from tide-gauge recordings alone. This is especially important for open-ocean regions (e.g., the Atlantic coast of Africa and South America) for which there are very few available data. Because tsunami wave dynamics in deep water are linear to first order, the square of the tsunami wave height in the open ocean is directly proportional to the energy of the waves. As a consequence, the distribution of computed maximum open-ocean wave amplitudes are also patterns of tsunami energy propagation (Fig. 1). Although the nearshore wave dynamic is simplified in this model as a result of insufficient
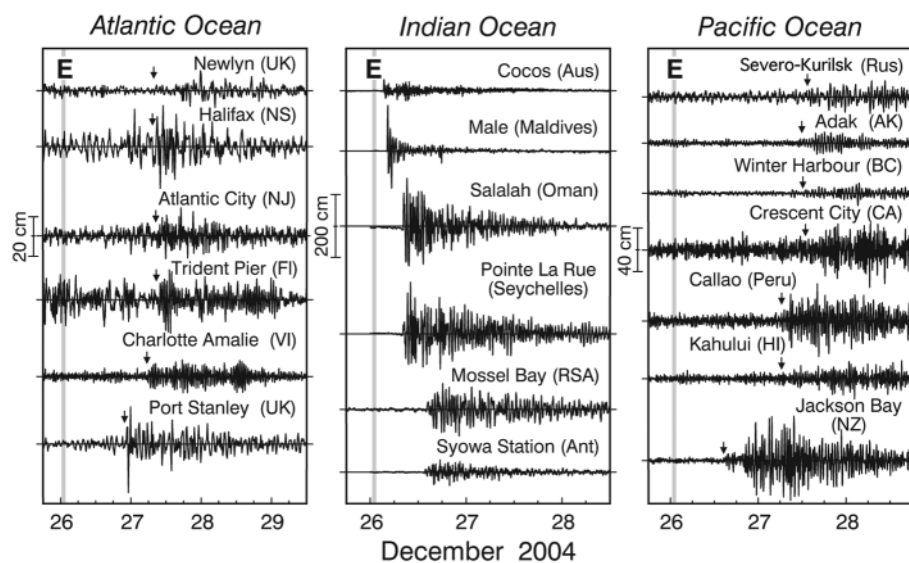


**Fig. 2.** Time series of tsunami wave heights (cm) as recorded at selected tide-gauge stations in the three major ocean basins. Arrows indicate first arrival of the tsunami.

resolution, the maximum computed offshore amplitudes provide accurate estimates, because these maximum values are hardly influenced by coastal reflections and, therefore, by model inaccuracies nearshore. The model offshore amplitude distribution matches very well the amplitude variation along coastal tide-gauge records. In particular, we note that the anomalously high coastal amplitudes observed in far-field regions

closely correspond to the predominant directions of tsunami energy propagation. Halifax (Canada), Manzanillo (Mexico), Callao (Peru), and Arica (Chile) all recorded wave amplitudes >50 cm, and each site is located at the terminus of a beam of computed tsunami energy that extends more than 20,000 km from the source region.

Our model results support suggestions that there are two main factors affecting tsunami
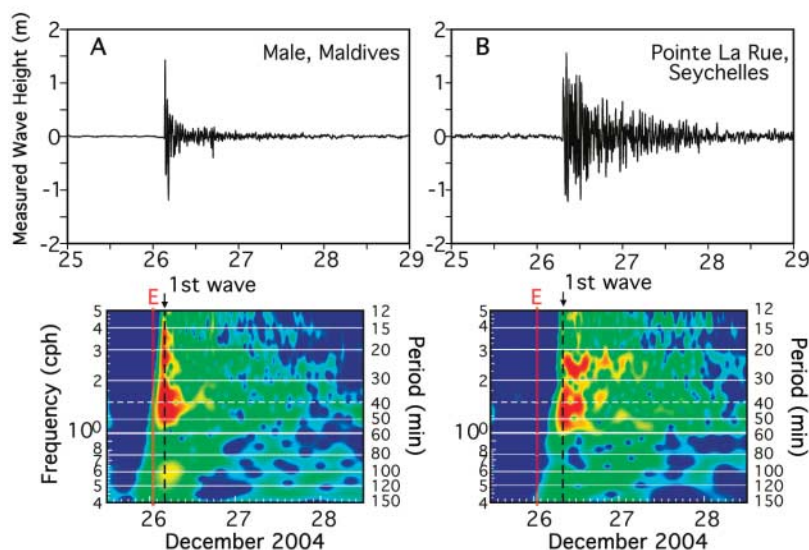
**Fig. 3.** Wavelet analysis of tsunami wave heights recorded by tide gauges at (**A**) Male, Maldives and (**B**) Pointe La Rue, Seychelles. Each plot shows the first 60 hours of the observed tsunami record and its corresponding wavelet decomposition (frequency/period versus time).

wave directionality: the focusing configuration of the source region (*15*) and the waveguide structure of mid-ocean ridges (*16*). Continental shelves also act as waveguides (*17*) and were apparently responsible for alongshore propagation and persistent "ringing" for the Pacific coasts of South and North America. In the near field, the focusing effect of the large extension of the earthquake source region was the primary factor determining directionality of the 2004 Sumatra tsunami. The long and narrow initial seafloor deformation generated waves with highest amplitudes propagating in the cross-source (here, zonal) direction, with smaller energy waves propagating in the long-source (meridional) direction. This effect is evident in both the model and tide-gauge data.

For far-field waves, seafloor topography is the main factor determining the directionality of energy propagation. Analysis of the Sumatra tsunami model (Fig. 1 and movie S1) illustrates the role of mid-ocean ridges in guiding interocean tsunami propagation. The Southwest Indian Ridge and the Mid-Atlantic Ridge served as waveguides for tsunami energy propagation into the Atlantic Ocean, whereas the Southeast Indian Ridge, Pacific-Antarctic Ridge, and East Pacific Rise served as guides for waves entering the Pacific. Results further show that ridges act as wave guides only until their curvature exceeds critical angles at locations along the tsunami wave paths. For example, the sharp bend of the Mid-Atlantic Ridge in the South Atlantic results in the tsunami ray leaving the waveguide near 40° S and hitting the Atlantic coast of South America with relatively high wave amplitudes. The model predicts the large (~1 m) peak waves observed at Rio de Janeiro (Brazil), but model verification for other locations on the east coast of South America is hampered by

lack of instrumentation (Fig. 1). Focusing by the Ninety-East Ridge beamed tsunami energy southward toward the coast of Antarctica. There were no gauge stations on the coast of Antarctica directly in line with the beam of tsunami energy arriving from the Ninety-East Ridge, and only moderate (60 to 70 cm) peak-to-peak waves were recorded at the French Dumont d'Urville station (*18*) and the Japanese station Syowa on the coast of Antarctica. These sites were more than 2000 km to the east and west, respectively, of where our model predicts maximum coastal tsunami waves due to focusing by the Ninety-East Ridge.

For most of the eastern and central Indian Ocean records, the first few waves were the largest (up to 12 hours of anomalously high wave intensity), followed by relatively rapid exponential wave attenuation. Model simulations illustrate that these records are from locations where the largest tsunami waves followed a direct route from the source after initial focusing by the source configuration. This is consistent with source-focusing as the main factor determining evolution of the tsunami in the near field (*19*).

Tide-gauge recordings from the western Indian and other oceans show increased tsunami duration, with maximum waves arriving later in the first wave train. This demonstrates increased input from waves that reached the gauge locations after scattering or refracting from shallow submarine features and reflecting from the coasts. In the case of topographic effects, the multiple refraction and slower propagation of waves constrained by the mid-ocean ridge waveguides led to both the later arrival of the largest amplitude waves and the prolonged duration of tsunami activity associated with distinct bathymetric features. The records

for Male in the Maldives and Pointe La Rue in the Seychelles (Fig. 3) serve to illustrate the two different types of tsunami wave patterns. The Male tide gauge recorded a large first wave with rapid amplitude decay thereafter (Fig. 3A), whereas the Pointe La Rue gauge (Fig. 3B) recorded a more complex pattern with substantially slower amplitude decay. Wavelet transforms (*20*) for these data emphasize the more limited duration and higher frequencies of the Male record (~1 day duration, 15- to 50-min periods) compared with the Pointe La Rue record (~3 day duration, 20 to 60 min periods). Male is directly across from the source region with no shallow scatterers in between, whereas Pointe La Rue received both scattered waves (through the Maldives and Chagos Archipelago) and reflected waves (e.g., off the Africa and Madagascar coasts).

The prolonged tsunami records for the Atlantic Ocean (Fig. 2 and fig. S2A) are consistent with substantial tsunami energy propagation along the Mid-Atlantic Ridge waveguide. In the Pacific Ocean, wave trains for the Sumatra tsunami often contained two or more distinct "packets" (Fig. 2 and fig. S2B) with different spectral characteristics. Our model provides a few explanations for this behavior. First, waveguide-driven tsunami dynamics give rise to two packets of waves: one packet of relatively small-amplitude, faster waves that took a direct path across the deeper regions of the ocean and another packet of typically higher amplitude, slower waves that traveled along ridge topographic waveguides.

Because it is so vast, the Pacific Ocean allows for two different propagation paths for most coastal locations. It is also possible that individual wave packets underwent multiple reflections from continental coastlines. Lastly, the packet structure in the Pacific records could be due to leakage of tsunami energy into the Pacific from the Atlantic Ocean. Our model shows (movie S1) tsunami waves propagating through the Drake Passage between South America and Antarctica, with amplitudes comparable with the waves that propagated directly into the Pacific from the west, i.e., from the Indian Ocean. Waves from the Atlantic arrived later at most locations in the Pacific, except for southern Chile, where the waves from the Atlantic arrived first.

Although no direct tsunami damage has been reported for the 2004 event outside the Indian Ocean basin, our study demonstrates the ability for energy from localized earthquakes to be transported throughout the world ocean. Thus, large tsunamis can propagate substantial and damaging wave energy to distant coasts, including different oceans, through a combination of source focusing and topographic waveguides. Local resonant effects may strongly amplify the arriving waves, as occurred during the 1964 Alaska tsunami in Port Alberni, British Columbia, and during the

1960 Chile tsunami in the Magadan region on the northwestern coast of the Sea of Okhotsk.

### References and Notes

1. S. Stein, E. A. Okal, *Nature* **434**, 581 (2005).
2. R. Bilham, *Science* **308**, 1126 (2005).
3. C. Subarya *et al.*, *Eos Trans. AGU* **86**, U51A (2005).
4. The Cocos Islands gauge is maintained by the National Tidal Centre of the Australian Bureau of Meteorology.
5. P. Liu *et al.*, *Science* **308**, 1595 (2005).
6. V. V. Titov, C. E. Synolakis, *Geophys. Res. Lett.* **24**, 1315 (1997).
7. Here, we use "amplitude-sensitive" tsunami arrival time estimation because it is more accurate than travel-time algorithms that do not take into account wave amplitude. The tsunami travel times contoured in Fig. 1 are inferred from arrival times for the smallest waves simulated by the MOST tsunami propagation model. The areas without contours delineate regions where arrival times are difficult to estimate because waves of similar small amplitudes arrive at different times from different "packets" and from prolonged wave trains. This creates multivalue arrival times for some locations, reflecting the difficulties in determining tsunami arrival at tide-gauge records with small initial wave amplitudes.
8. J. Gower, *Eos* **86**, 37 (2005).
9. W. Smith, R. Scharroo, V. Titov, D. Arcas, B. Arbic, *Oceanography* **18**, 10 (2005).
10. V. V. Titov, C. E. Synolakis, *J. Waterways Ports Coastal Ocean Eng.* **124**, 57 (1998).
11. C. J. Ammon *et al.*, *Science* **308**, 1133 (2005).
12. K. Hirata, in preparation.
13. V. V. Titov, H. O. Mofjeld, F. I. Gonzalez, J. C. Newman, in *Tsunami Research at the End of a Critical Decade*, G. T. Hebenstreit, Ed. (Kluwer Academic Publishers, Amsterdam, 2001), pp. 75–90.
14. At the time of the initial simulation, the preliminary estimate of the earthquake magnitude was $M_w = 8.5$, representing a release of energy lower by a factor of 16 than the final estimate of $M_w = 9.3$. The only direct tsunami measurement available was for the Cocos Islands. This record provided the initial scaling for the initial specification of the tsunami source, modeled as the instantaneous seafloor deformation of the aftershock area, corresponding to a 1200-km-long rupture along the Sunda Trench. This initial tsunami source length and the resulting magnitude differed substantially from the much shorter rupture length and lower magnitude indicated by the preliminary seismic analysis. However, the resulting model simulations agreed qualitatively with the early tsunami observations. Later seismic analyses (*11*) have confirmed the larger earthquake magnitude and source region.
15. An. G. Marchuk, V. V. Titov, in *Proc. IUGG/IOC International Tsunami Symposium*, Novosibirsk, USSR (1989), pp. 11–17.
16. S. Koshimura, F. Imamura, N. Shuto, *Coastal Eng. J.* **41**, 167 (1999).
17. F. I. González, K. Satake, E. F. Boss, H. O. Mofjeld, *Pure Appl. Geophys.* **144**, 409 (1995).
18. Sea-level records for Dumont d'Urville are available as part of the French ROSAME (Réseau d'Observation Sub-antarctique et Antarctique du niveau de la Mer) Antarctica and South Indian Ocean Tide Gauge Network. Plots for the tsunami arrival on 26 December 2004, were provided by Laurent Testut (Laurent.Testut@notos.cst.cnes.fr).
19. Here, "near field" for this major tsunami encompasses almost all of the Indian Ocean.
20. Wavelet transforms determine the variation in signal intensity within a hierarchy of frequency bands as a function of time (*21*).
21. W. J. Emery, R. E. Thomson, *Data Analysis Methods in Physical Oceanography* (Elsevier Science, ed. 2, Amsterdam, 2001).
22. We thank the numerous scientists and agencies who contributed the tide-gauge observations reported in this paper and P. Kimber for drafting the figures. We also thank the four reviewers for their constructive suggestions and criticism. This research was partially funded by the Joint Institute for the Study of the Atmosphere and Ocean (JISAO) under NOAA Cooperative Agreement NA17RJ1232 and by the Department of Fisheries and Oceans, Canada. JISAO Contribution 1136; PMEL Contribution 2809.

# Dating of Multistage Fluid Flow in Sandstones

**Darren F. Mark,**[1]* **John Parnell,**[1] **Simon P. Kelley,**[2] **Martin Lee,**[3] **Sarah C. Sherlock,**[2] **Andrew Carr**[4]

Through ultraviolet laser argon-argon dating of potassium feldspar cements containing fluid inclusions, we determined temperature-composition-time data for paleofluids in a sedimentary basin, including data for an evolving episode of fluid flow recorded in distinct phases of cement. The fluid evolved from mixed aqueous oil 83 million years ago to purely aqueous by 76 million years ago, thus dating the time of oil charge in this reservoir.

The dating of fluid movement (*1*) on continental shelves and in sedimentary basins is critical to the prediction of the distribution of natural resources, including hydrocarbons, water, and metalliferous ore deposits. For example, accurately establishing the direct timing of oil migration within a sedimentary basin could ultimately lead to enhanced oil discovery. However, only indirect dating has been possible by using the age of minerals that predate or postdate oil charge (*2–4*), by using fluid temperatures to predict the timing of entrapment from burial history plots (*5*), and by theoretical prediction of oil generation from heat-flow models (*6*).

Characterization of fluid inclusions within K-feldspar cement (*7*) in sandstones permits the integration of homogenization temperature (*8*) data with high-resolution Ar-Ar ages (*9*), as long as the basin thermal history does not disturb the Ar isotope system. If such temperature-composition-time (*T-X-t*) points can be determined for K-feldspar overgrowths containing oil inclusions, we can directly constrain episodes of oil migration and accumulation. In conjunction with basin modeling, detailed chronologies can be established to relate oil generation and charge into the reservoir. We demonstrate the potential of this approach by using rocks from the Faeroe-Shetland Basin (*10*).

The Victory gas field is 48 km northwest of the Shetland Isles (Fig. 1A, Block 207/1a). Lower Cretaceous reservoir rocks rest unconformably on Lewisian basement. Although now the Victory field is filled with gas, oil migrated into it episodically during the Late Cretaceous period and the Paleocene epoch (*11*). The lower part of the sedimentary succession (well 207/1a-5, 1463 to 1466 m) consists of oil-stained, poorly sorted conglomerate with a sandy matrix. The matrix is cemented by quartz, calcite, kaolinite, pyrite, and K-feldspar. The authigenic K-feldspar (>99% orthoclase, table S1) consists of overgrowths (100 to 500 μm) around detrital grains (cores) of replaced plagioclase and pristine K-feldspar (Fig. 2A), as well as idiomorphic crystals (100 to 200 μm) (Fig. 2B).

K-feldspar overgrowths exhibit a discrete fluid-inclusion zonation pattern, which is delineated by phase and composition variations (Fig. 3). Three distinct fluid inclusion assemblages are seen (*10*).

Primary two-phase oil and aqueous fluid inclusions delineate zone 1. Fluid inclusions are randomly dispersed along the core-overgrowth contact, extending ~25 to 75 μm into the overgrowth, away from the core-overgrowth interface. Aqueous fluid inclusions are 5 to 15 μm across. Oil fluid inclusions are 4 to 10 μm across and fluoresce blue under ultraviolet (UV) light. Fluid entrapment for both compositions occurred between 108° and 125°C [$n = 106$ homogenization temperature ($T_h$) measurements]. Zone 2 occupies the midsection of the overgrowth, solely containing primary two-phase aqueous fluid inclusions. The zone is 50 to 200 μm thick; inclusions are 5 to 10 μm in diameter; and the fluids were trapped between 86° to 108°C ($n = 78$). Zone 3 extends out from zone 2 to the overgrowth edge and is 20 to 100 μm thick, although dissolution at the outer margin suggests it was once larger. Zone 3 inclu-

[1]Department of Geology and Petroleum Geology, Meston Building, Meston Walk, University of Aberdeen, Aberdeen, AB24-3UE, UK. [2]Centre for Earth, Planetary, Space and Astronomical Research (CEPSAR), Department of Earth Sciences, Open University, Walton Hall, Milton Keynes, MK7-6AA, UK. [3]Division of Earth Sciences, Centre for Geosciences, Lilybank Gardens, University of Glasgow, Glasgow, G12-8QQ, UK. [4]Advanced Geochemical Systems Ltd., Towles Fields, Burton on the Wolds, Leicestershire, LE12-5TD, UK.

*To whom correspondence should be addressed. E-mail: d.mark@abdn.ac.uk